

Towards scalable multi-qubit optimal control via interaction decomposition in the diagonal frame

Bora Baran,^{1,2,*} Tommaso Calarco,^{1,2,3} Matthias M. Mueller,¹ and Felix Motzoi^{1,2}

¹*Forschungszentrum Jülich, Institute of Quantum Control,
Peter Grünberg Institut (PGI-8), 52425 Jülich, Germany*

²*Institute for Theoretical Physics, University of Cologne,
Zuelpicher Strasse 77, 50937 Cologne, Germany*

³*Dipartimento di Fisica e Astronomia, Università di Bologna, 40127 Bologna, Italy*

In this work, we introduce a general n -qubit formulation of control objectives that allows a control target to be specified in a diagonal frame, so that only the diagonal entries must be characterized, thus quadratically reducing the complexity of the cost functional in contrast to a full target matrix. We do so by representing any n -qubit unitary transformation as a diagonal phase map on the computational basis states, as they are naturally diagonalizable by unitarity. By using discrete derivative operators to analytically construct support-selective phase invariants, we enable to deterministically isolate and quantify any multi-qubit interactions encoded in the phase map. These phase invariants form a coordinate system for the formulation of specific control targets in terms of arbitrary desired multi-qubit interactions, solely relying on the experimentally accessible diagonal phases. To illustrate the framework, we synthesize two genuinely tripartite entangling gates, both, diagonal and non-diagonal. These are obtained with a single shaped microwave pulse, for a numerically simulated room-temperature nitrogen-vacancy center with a three qubit nuclear spin register, with durations of about a microsecond. These results represent a factor 10-100 reduction in operation time compared with the fastest existing NV-based entanglers that act on more than two qubits at once.

I. INTRODUCTION

One of the key factors enabling quantum computing is the ability to control qubits with high precision and speed. To this end, quantum optimal control provides systematic methods for shaping external fields to steer a quantum system through a desired transformation in a way that enables precise implementation of logical gates, state transfers, and error-resilient operations [1]. As a result, quantum optimal control has become a central tool for engineering high-performance operations in quantum technologies, from trapped ions and superconducting circuits to solid-state spin qubits [2–15].

Established frameworks such as GRAPE [16–19], Krotov [20–22], CRAB [23–26], and various other methods cast the optimization task in a general form, expressing the control problem as the minimization of a cost functional that quantifies the deviation between the realized and the desired evolution, independent of the specific choice of controls [9, 16, 21–23, 27–34]. This allows to improve the effective dynamics of applied controls towards desired transformations, given that accurate feed-forward from the system is accessible. However, full process or state tomography scales exponentially with the number of qubits and requires a large number of measurement settings [35]. Meanwhile, as the number of qubits increases, the control landscape becomes exponentially larger, the relevant interactions become increasingly intertwined, and it becomes thereby harder to fulfill

targets [1, 30, 36]. These challenges indicate the need for scalable and flexible control objectives that still capture the desired interaction content of a target operation.

A control framework which relies only on feed-forward from a subset of parameters so that it requires less characterization is therefore of particular interest, for example, selective phase estimation, partial tomography, or stabilizer-based reconstruction [22, 35, 37–40]. For example, if we needed to only characterize the diagonal entries of a unitary transformation operator, because the diagonal of a unitary has only 2^n independent degrees of freedom, one phase for each computational-basis state, so determining its diagonal scales as $\Theta(2^n)$, unlike a general n -qubit unitary, which has $\Theta(4^n)$ degrees of freedom and requires full process tomography to characterize [35, 41]. To benefit from this scaling advantage, it would require a method completely transform any unitary into the diagonal and another method to decompose its interaction structure that became encoded into its diagonal phase map. Considering that any unitary operation admits a diagonal representation in an appropriate basis [41, 42], we already have a solution for the first issue. What is left to solve, is a way to isolate and quantify any k -body interactions that became encoded into the diagonal representations phase map, without having to invert the unitary back.

In this work we analytically derive a way for deterministically isolating and quantifying any multi-qubit interactions, invariant to other contributions encoded in the diagonal phase map, from the phase map, without having to invert the diagonal frame. We use as a foundation, that any n -qubit unitary in a diagonal form

* b.baran@fz-juelich.de

is fully characterized by its a real-valued *phase map* acting on the binary variable based basis states. To probe mutual dependencies of the phase onto a subset of qubits, we flip through each configuration of the qubits of interest and compare to the original value of the phase map. Each act of flipping a binary configuration and comparing the resulting value of the function, corresponds to the use discrete derivative operators, natural discrete analogues of derivatives usually found in boolean analysis [43]. To make the effect of these discrete derivatives on the diagonal phase map explicit, we invoke that any real valued function on the binary hypercube, here corresponding to qubit basis states, can be given in a Walsh Hadamard representation[43–45]. By appropriately combining these discrete derivatives to obtain *phase invariants*, quantities that deterministically isolate k -body interaction terms for any subset of qubits of the multi-qubit transformation, fully invariant to all other contributions encoded on the phase map. This naturally generalizes the idea of local invariants, i.e. 1-body invariants in our language, and permits the creation of general maps where different interactions are separately controlled, or left as arbitrary gauges [31, 46–48].

These *phase invariants* not only enables to do quantum optimal control requiring only a subset of parameters to characterize, being the diagonal, but also enable the exact specification of any desired k -local structure as a control target, to be induced by the control pulse solely based on diagonal-frame characterization. Besides that, this also solves the issue of over-constraining the optimization target with physically irrelevant collateral targets, as this framework allows to leave physically irrelevant degrees of freedom unspecified, for the optimizer to exploit. Thus, such a formulation of control targets, allows to optimize for specific unitary transformations with reduced optimization overhead, next to cost efficient characterization, and invariant to unspecified contributions, making it an excellent candidate for the synthesis of complex multi-qubit gates in closed loop scenarios.

The nitrogen-vacancy (NV^-) center in diamond provides an ideal solid-state platform for this framework [49, 50]. It combines an optically addressable electronic spin with nearby ^{13}C and ^{14}N nuclear spins that exhibit stable, hyperfine-mediated interactions, and all of this at room-temperature [51]. These couplings naturally support diagonal multi-spin correlations, making the NV register particularly suited for phase map based synthesis of both diagonal and non-diagonal multi-qubit entanglers. Using this structure, we demonstrate the synthesis of two tripartite entangling gates in a simulated NV^- - ^{14}N - ^{13}C - ^{13}C register: (i) a canonically diagonal $e^{i(\pi/4)Z \otimes Z \otimes Z}$ entangler with process fidelity $F_{ZZZ} = 0.9978$, and (ii) a non-diagonal $e^{-i(\pi/4)X \otimes Z \otimes Z}$ entangler realized by optimization in a diagonalizing (Hadamard-sandwiched) frame, reaching

$F_{XZZ} = 0.9985$. Our k -body-interaction-resolved synthesis induces genuine tri-entangling gates via microwave pulses of only $1.25\mu s$ and $1.5\mu s$, which represents a factor 10 – 100 reduction in operation time compared with the fastest existing NV-based multi-qubit entanglers that act on more than two qubits at once [52–54].

II. THEORY OF PHASE INVARIANTS

A. Preliminaries

In this section we introduce the preliminary tools that prepare the ground for the main results in this work. We show how any n -qubit unitary transformation can be characterized by a diagonal phase map. Next, we introduce a specific representation of the phase map. And at last, we present a derivative analog, which can be applied to such phase maps to probe the interaction terms encoded in it.

1. Diagonal Phase Map

Any n -qubit unitary operator U_{target} is diagonalizable [41], i.e., there exists a unitary transformation V such that

$$U_{\text{diag}} = V U_{\text{target}} V^\dagger = \sum_{\vec{x} \in \{0,1\}^n} e^{i\phi(\vec{x})} |\vec{x}\rangle \langle \vec{x}|. \quad (1)$$

While such a diagonalizing transformation need not be local, many operations of practical relevance in quantum control, such as gates generated by Pauli-product Hamiltonians, including multi-qubit interaction terms—are locally diagonalizable and naturally admit a description in this form [42]. In this representation, the phase map $\phi(\vec{x})$ is experimentally available as the phases $\{\phi(\vec{x})\}_{\vec{x} \in \{0,1\}^n}$ of the unitary’s diagonal entries and fully characterizes the transformation within the chosen frame.

As a simple example, we consider the two-qubit unitary $U_{Z \otimes Z} = e^{i\gamma Z \otimes Z}$, and recall that $Z|x\rangle = z_x|x\rangle$ with $z_0 = +1$ and $z_1 = -1$. Thus

$$(Z \otimes Z) |x_1 x_2\rangle = (z_{x_1} z_{x_2}) |x_1 x_2\rangle, \quad (2)$$

and consequently

$$e^{i\gamma Z \otimes Z} |x_1 x_2\rangle = e^{i\gamma z_{x_1} z_{x_2}} |x_1 x_2\rangle. \quad (3)$$

We therefore can directly see that a *phase map* such as

$$\phi(x_1, x_2) = \gamma z_{x_1} z_{x_2} \quad (4)$$

allows to fully characterize the underlying two-body interaction, as a function of the qubit configuration

$$\vec{x} = (x_1, x_2).$$

This allows to represent $U_{\mathbf{Z} \otimes \mathbf{Z}}$ as

$$U_{\mathbf{Z} \otimes \mathbf{Z}} |x\rangle = e^{i\phi(\vec{x})} |x\rangle, \quad (5)$$

where the multi-qubit interaction structure of $U_{\mathbf{Z} \otimes \mathbf{Z}}$ is encoded directly in the dependence of $\phi(\vec{x})$ on the n -qubit configuration in the computational basis $\vec{x} = (x_1, \dots, x_n)$ with $x_i \in \{0, 1\}$.

More generally, a *phase map* $\phi(\vec{x})$ can be used to completely characterize any unitary transformation U_{diag} in the computational basis, so that we can write [44]:

$$\phi : \{0, 1\}^n \rightarrow \mathbb{R}/2\pi\mathbb{Z}, \quad U_{\text{diag}} |x\rangle = e^{i\phi(\vec{x})} |x\rangle. \quad (6)$$

2. Walsh Hadamard Expansion

Next, we consider that such a phase map $\phi(\vec{x})$ is simply a real-valued function on the Boolean cube $\{0, 1\}^n$; it therefore admits a standard representation in terms of Boolean Fourier analysis [43, 45]. In particular, any real-valued function on $\{0, 1\}^n$ has a unique expansion in the $\{\pm 1\}$ -valued characters, known as the Walsh-Hadamard expansion [44]:

$$\phi(\vec{x}) = \sum_{S \subseteq \{1, \dots, n\}} \widehat{\phi}(S) \chi_S(\vec{x}). \quad (7)$$

In each term, the coefficients $\widehat{\phi}(S)$ represent the real-valued phase contributions supported on the subset of qubits S and are given by the Walsh-Hadamard transform

$$\widehat{\phi}(S) = 2^{-n} \sum_{\vec{x} \in \{0, 1\}^n} \phi(\vec{x}) \chi_S(\vec{x}), \quad (8)$$

whereas the Walsh characters $\chi_S(\vec{x})$ provide the sign value for each term and are defined as

$$\chi_S(\vec{x}) = \prod_{i \in S} z_{x_i}, \quad z_{x_i} = (-1)^{x_i}. \quad (9)$$

Here, it is important to notice that $\chi_S(\vec{x})$ depends only on the configurations x_i of qubits indexed by S .

Grouping the terms in the Walsh-Hadamard expansion (7) by the size of their supports $|S| = k$ produces a hierarchical k -body decomposition and makes the given interaction

order more explicit,

$$\begin{aligned} \phi(\vec{x}) &= \widehat{\phi}(\emptyset) \\ &+ \sum_i \widehat{\phi}(\{i\}) \chi_{\{i,j\}}(\vec{x}) \\ &+ \sum_{i < j} \widehat{\phi}(\{i, j\}) \chi_{\{i,j\}}(\vec{x}) \\ &+ \sum_{i < j < \ell} \widehat{\phi}(\{i, j, \ell\}) \chi_{\{i,j,\ell\}}(\vec{x}) \\ &+ \dots + \widehat{\phi}(\{1, \dots, n\}) \chi_{\{1, \dots, n\}}(\vec{x}). \end{aligned} \quad (10)$$

This subset-indexed decomposition resembles the standard synthesis of diagonal unitaries into multi-controlled phase gates [44]. However, rather than focusing on a circuit-level construction, our approach works generally with the phase map ϕ and its Walsh-Hadamard coefficients $\widehat{\phi}(S)$, providing a functional characterization of the k -body contributions independent of any specific gate decomposition.

3. Discrete Derivatives

The discrete derivative operator originally stems from the analysis of Boolean functions and provides a derivative for discrete functions on the binary hypercube [43]. Here, we define for each qubit index $i \in \{1, \dots, n\}$ the normalized *single qubit discrete derivative operator*, as

$$(\delta_i \phi)(x_1, \dots, x_n) := \frac{1}{2} [\phi(x_1, \dots, x_{i-1}, 1, \dots, x_n) - \phi(x_1, \dots, x_{i-1}, 0, \dots, x_n)], \quad (11)$$

to be able to probe the change of the phase value $\phi(\vec{x})$ for a specific n -qubit configuration $\vec{x} = (x_1, \dots, x_n)$ (in the computational basis), considering the case when the i -th qubit is flipped. We added the normalization factor $1/2$ to ensure that δ_i also acts analog to a discrete derivative with respect to the binary variable x_i on the phase map.

To probe phase changes resulting from simultaneous flips of multiple qubits, and thereby the mutual dependencies of a subset of qubits $S \subseteq \{1, \dots, n\}$, we further define the *multi-variable discrete derivative operator*

$$\delta_S = \prod_{i \in S} \delta_i, \quad (12)$$

obtained by applying the corresponding single-qubit discrete derivatives successively. Since the operators δ_i commute trivially, the order of application is not important.

In the following section, we show how these multi-variable discrete derivative operators can be used to construct quantities that deterministically isolate the genuine multi-qubit interactions encoded in the diagonal phase maps of arbitrary n -qubit unitary transformations.

B. Phase Invariants

In this section, we show how the tools introduced in the previous section allow to construct *phase invariants* that act as support-selective filters on the phase map $\phi(\vec{x})$ of any diagonalized unitary transformation, enabling the deterministic isolation and quantification of specific multi-qubit interaction components.

We begin by showing how the action of the multi-variable discrete derivative δ_S (12) on a phase function $\phi(\vec{x})$ filters out all phase contributions that do not depend on every qubit in S . This becomes transparent when expressing the phase map $\phi(\vec{x})$ in its Walsh-Hadamard expansion (7).

We note that each single-qubit discrete derivative δ_i defined in (11) is a linear operator. And since these operators trivially commute, the multi-variable discrete derivative δ_S which consists of successive single-qubit discrete derivatives, as defined in (12), is also linear. Therefore it suffices by linearity to show the action of δ_S on a single term $\widehat{\phi}(R)\chi_R(\vec{x})$ appearing in the Walsh-Hadamard expansion of $\phi(\vec{x})$.

Since $\widehat{\phi}(R)$ is constant with respect to \vec{x} , we may factor it out:

$$\delta_S[\widehat{\phi}(R)\chi_R(\vec{x})] = \widehat{\phi}(R)\delta_S[\chi_R(\vec{x})], \quad (13)$$

and thereby focus only on what happens to the Walsh character $\chi_R(\vec{x})$.

If the Walsh character does not depend on a qubit i (i.e., $i \notin R$), then flipping x_i via the corresponding single-qubit discrete derivative δ_i in δ_S leaves $\chi_R(x)$ unchanged, so that the term is subtracted from itself and vanishes:

$$\delta_i[\chi_R(x)] = \frac{1}{2}[\chi_R(x_i = 1) - \chi_R(x_i = 0)] = 0. \quad (14)$$

If instead $i \in R$, then the character changes sign when x_i is flipped. In this case $\chi_R(x)$ can also be written as $\chi_R(x) = z_{x_i}\chi_{R \setminus \{i\}}(x)$, so that we obtain

$$\begin{aligned} \delta_i[\chi_R(x)] &= \frac{1}{2}[(-1)\chi_{R \setminus \{i\}} - (+1)\chi_{R \setminus \{i\}}] \\ &= -\chi_{R \setminus \{i\}}(x), \end{aligned} \quad (15)$$

and the dependence on qubit i via the term z_{x_i} in the Walsh character is no longer present while leaving the remaining support intact with only a flipped sign. Hence we can write

$$\delta_i[\chi_R] = \begin{cases} 0, & i \notin R, \\ -\chi_{R \setminus \{i\}}, & i \in R. \end{cases} \quad (16)$$

As the multi-variable discrete derivative δ_S corresponds to the application of several discrete derivatives on the subset S successively, one can conclude for the multi-variable discrete derivative the following.

Proposition 1 (Support Inclusion Filtering). *Let $S, R \subseteq \{1, \dots, n\}$. Then the action of the multi-variable discrete derivative operator δ_S on a Walsh character χ_R is given by*

$$\delta_S[\chi_R] = \begin{cases} 0, & S \not\subseteq R, \\ (-1)^{|S|}\chi_{R \setminus S}, & S \subset R \\ (-1)^{|S|}, & S = R. \end{cases} \quad (17)$$

Thus, the action of the multi-variable discrete derivative δ_S on a phase function $\phi(\vec{x})$ annihilates all Walsh characters whose support does not contain S , while it reduces those whose support strictly contains S to a character supported on $R \setminus S$, and leaves those whose support is exactly S (up to a sign). However, δ_S does not eliminate terms whose support contains S *together with additional qubits*. To isolate phase contributions supported *exactly* on S , these remaining terms must be removed.

Remark 1. For any $S \subseteq \{1, \dots, n\}$ we denote the complement by $\bar{S} := \{1, \dots, n\} \setminus S$, and write computational basis configurations as $\vec{x} = (x_S, x_{\bar{S}})$, grouping qubit assignments on S and \bar{S} respectively.

For the purpose of further filtering out terms supported on S *together with additional qubits* in $\phi(\vec{x})$ by effectively subtracting them by themselves, we define the averaged mixed difference

$$\frac{1}{2^{|\bar{S}|}} \sum_{x_{\bar{S}} \in \{0,1\}^{\bar{S}}} \delta_S[\phi(x_S, x_{\bar{S}})], \quad (18)$$

which averages $\delta_S\phi$ over all configurations of complementary qubits. The prefactor $2^{-|\bar{S}|}$ normalizes the average so that a term supported *exactly* on S survives with coefficient $(-1)^{|S|}$ and is not amplified.

To understand how (18) eliminates all terms whose support contains S *together with additional qubits*, we expand ϕ again in its Walsh-Hadamard form (7). Since both δ_S and the averaging are linear, it suffices to analyze the effect on a single Walsh term $\widehat{\phi}(R)\chi_R(\vec{x})$ with $R \setminus S \neq \emptyset$. Factoring out the constant coefficient $\widehat{\phi}(R)$, we are left with the average over $\delta_S\chi_R$.

By Proposition 1, if $R \supset S$ with $R \neq S$, then

$$\delta_S[\chi_R(x_S, x_{\bar{S}})] = (-1)^{|S|}\chi_{R \setminus S}(x_{R \setminus S}), \quad (19)$$

a reduced Walsh character supported on $R \setminus S$. If $R \setminus S$ contains a single qubit j , then $\chi_{R \setminus S}(x_{R \setminus S}) = z_{x_j}$ and

$$\frac{1}{2} \sum_{x_j \in \{0,1\}} z_{x_j} = \frac{1}{2}[(+1) + (-1)] = 0. \quad (20)$$

If instead $|R \setminus S| > 1$, then $\chi_{R \setminus S}(x_{R \setminus S}) = \prod_{j \in R \setminus S} z_{x_j}$,

and the average factorizes:

$$\frac{1}{2^{|R \setminus S|}} \sum_{x_{R \setminus S}} \chi_{R \setminus S}(x_{R \setminus S}) = \prod_{j \in R \setminus S} \left(\frac{1}{2} \sum_{x_j \in \{0,1\}} z_{x_j} \right) = 0. \quad (21)$$

Since $R \setminus S \subseteq \bar{S}$, this vanishing factor appears in the full average (18), making the contribution vanish identically.

Any Walsh character whose support contains S and additional qubits depends on at least one qubit outside of S , that is, on a qubit indexed by \bar{S} . By this argument, it therefore suffices to average the multi-variable discrete derivative $\delta_S \phi(x_S, x_{\bar{S}})$ over all configurations $x_{\bar{S}} \in \{0,1\}^{\bar{S}}$ in order to eliminate all such possible contributions, without prior knowledge of their existence in an arbitrary phase map $\phi(\vec{x})$. This allows to conclude the following.

Proposition 2 (support-selective phase invariants). *For any $S \subseteq \{1, \dots, n\}$,*

$$\Delta_S(\phi) := \frac{1}{2^{|\bar{S}|}} \sum_{x_{\bar{S}} \in \{0,1\}^{\bar{S}}} \delta_S[\phi(x_S, x_{\bar{S}})] \quad (22)$$

returns precisely the contribution to ϕ supported on S , and is invariant under adding any phase contribution supported on $R \neq S$.

Hence, $\Delta_S(\phi)$ acts as a perfect deterministic support filter: it removes all contributions not supported exactly on S and returns the interaction phase associated *exactly* with S .

In the following section, we show how these support-selective phase invariants, given by $\Delta_S(\phi)$, can further be used to formulate k -body interaction decomposed quantum optimal control targets.

C. Control Objectives on the Diagonal

In this section, we show how the phase invariants, which we derived in the previous section, enable to formulate k -body interaction decomposed control objectives for general n -qubit unitary transformations while relying only on information obtained from the characterization of their diagonal entries.

Firstly, it is convenient to use an alternating-sum representation of the phase invariants introduced in Section II B, which expresses each $\Delta_S(\phi)$ simply as a signed sum over the experimentally measurable phase values $\{\phi_x\}_{x \in \{0,1\}^n}$ of the unitary's gates diagonal entries. As shown in Appendix A, this representation reads

$$\Delta_S(\phi) = \frac{(-1)^{|S|}}{2^n} \sum_{x \in \{0,1\}^n} (-1)^{\sum_{i \in S} x_i} \phi(x), \quad (23)$$

and involves only phase values of computational-basis states that differ from the qubits in S .

For illustrative purposes, we consider a specific example of a three-qubit logical subspace with labels $\{a, b, c\}$. In a suitable diagonalizing frame, a diagonal three-qubit target unitary can be written in the form

$$U_{\text{diag}} = \exp \left(-i [\alpha_a Z_a + \alpha_b Z_b + \alpha_c Z_c + \gamma_{ab} Z_a Z_b + \gamma_{ac} Z_a Z_c + \gamma_{bc} Z_b Z_c + \lambda_{abc} Z_a Z_b Z_c] \right) \quad (24)$$

where the coefficients α_i , γ_{ij} , and λ_{ijk} parametrize the single-, two-, and three-body interaction phases, respectively. The nontrivial phase invariants associated with this three-qubit system are the seven quantities

$$\Delta_{\{a\}}, \Delta_{\{b\}}, \Delta_{\{c\}}, \Delta_{\{a,b\}}, \Delta_{\{a,c\}}, \Delta_{\{b,c\}}, \Delta_{\{a,b,c\}},$$

each defined as in Proposition 2. These phase invariants provide direct access to the corresponding interaction phases in Eq. (24). Explicit formulas for these phase invariants in terms of the diagonal phase values $\{\phi_x\}_{x \in \{0,1\}^3}$ are given in Appendix B.

Given the target values $\{\Delta_S^*\}_{S \subseteq \{a,b,c\} \setminus \emptyset}$ for the phase correlators, corresponding to desired values of interaction phases appearing in Eq. (24), we define the following phase invariant based control cost function.

Definition 1 (Support-Selective Phase Invariant based Control Objective (Three Qubits)).

$$\mathcal{J}_{3q} = \sum_{S \subseteq \{a,b,c\} \setminus \emptyset} w_{|S|} \left[1 - \cos(2(\Delta_S(\phi) - \Delta_S^*)) \right]. \quad (25)$$

This definition extends directly to an arbitrary number n of qubits by replacing $\{a, b, c\}$ with $\{1, \dots, n\}$ and summing over all nonempty subsets S .

The weights $w_{|S|}$ set the relative importance of $|S|$ -body interaction terms, allowing, for example, single-qubit or two-qubit contributions to be suppressed or emphasized depending on the control task. In many hardware platforms, the single-qubit weight w_1 may be set to zero, since local Z rotations are readily correctable.

The explicit factor of two in the control cost function (25), ensures π -periodicity in each phase invariant. This reflects the fact that Δ_S quantifies the interaction phase associated with diagonal Pauli- Z operators $Z_S = \prod_{i \in S} Z_i$. Shifting Δ_S by π flips only the sign of this interaction,

$$e^{-i(\Delta_S + \pi)Z_S} = -e^{-i\Delta_S Z_S}.$$

And this sign flip does not change the the physicality such as entanglement generation or nonlocal interaction strength. Thus, even though the numerical value of Δ_S might differ, the physical effect of the operation is equivalent. As a consequence, physically equivalent interaction

phases are identified by the cost function, while inequivalent ones are penalized. The resulting control cost func-

tion is invariant under non-selected contributions, interpretable in terms of well-defined interaction phases, and differentiable with respect to the underlying control parameters. Because the phase invariants $\Delta_S(\phi)$ are defined for arbitrary subsets S , the same construction extends immediately to general n -qubit systems, enabling k -body interaction decomposed optimization for any system size.

III. NUMERICAL DEMONSTRATIONS

A. System setup

a. Pulse Parametrization and Optimization The coherent manipulation of solid-state spin registers relies on external microwave (MW) control fields that drive transitions between coupled electronic and nuclear spins. In the NV center, such controls enable Hamiltonian engineering and noise-resilient quantum operations have been performed for specific use cases [15, 51, 55–60] primarily through temporal [9, 16, 21] and spectral [23, 32, 33] pulse shaping techniques. A control field can be expressed as a modulated carrier,

$$\begin{aligned} B(t) &= E(t) \cos(\omega_{\text{drive}} t), \\ E(t) &= w_\alpha(t) \sum_{i=1}^n a_i \cos(\omega_i t + \phi_i), \end{aligned} \quad (26)$$

where the envelope is parameterized by amplitudes a_i , frequencies ω_i , and phases ϕ_i . The multiplicative factor $w_\alpha(t)$, was added on top, and is a Tukey (tapered cosine) window that smoothly turns the pulse on and off,

$$w_\alpha(t) = \frac{1}{2} [1 - \cos(2\pi \frac{t}{T})] \quad \text{for } t \in [0, \alpha T], \quad (27)$$

and $w_\alpha(t) = 1$ in the flat region; $\alpha \in [0, 1]$ controls the taper fraction (we use $\alpha = 0.15$). This analytic form, used e.g. in CRAB [23, 24], GRAPE [16, 17] and combinations thereof [18, 28, 61, 62], defines a compact and experimentally compatible control parametrization vector to be optimized

$$(a_1, \dots, a_n, \omega_1, \dots, \omega_n, \phi_1, \dots, \phi_n). \quad (28)$$

b. Model Spin Hamiltonian This effective Hamiltonian serves as the working model for all control and simulation results. Its full derivation starting from the full laboratory-frame NV Hamiltonian is given in Appendix C. After applying the rotating-wave approximation (RWA)

near the electronic resonance, the Hamiltonian reads

$$\begin{aligned} H_{\text{NV}}^{(\text{RWA})}(t) &= \Omega \sum_{\mathbf{m}} [\sigma_x \cos(\Delta_e(\mathbf{m}) t) \sigma_y \sin(\Delta_e(\mathbf{m}) t)] \\ &\otimes |\mathbf{m}\rangle \langle \mathbf{m}| \Omega [\sigma_x \cos(\Delta_e t) - \sigma_y \sin(\Delta_e t)] \\ &- \Omega [q_x \sin(\Delta_e t) + q_y \cos(\Delta_e t)] \\ &\otimes \sum_i \theta_i [I'_{ix} \cos(\delta_i t - \phi_i) + I'_{iy} \sin(\delta_i t - \phi_i)] \end{aligned} \quad (29)$$

where the nuclear configuration index is $\mathbf{m} \equiv (m_N, \{m_{C_i}\})$, $\Omega = \gamma_e B_{1,\text{MW}}/\sqrt{2}$ is the MW control field, $\Delta_e = \omega_{\text{MW}} - \Lambda(\mathbf{m})$ is the MW detuning, with $\Lambda(\mathbf{m})$ being the configuration dependent electron frequencies (see Eq. (C14)), $\delta_i = \omega_i - \Lambda_s$ are the nuclear beat frequencies, with Λ_s being the electron transition frequency with Zeeman splitting, and θ_i, ϕ_i denote the local hyperfine misalignment angles. We set the carrier frequency ω_{drive} , given in the pulse parameterization in Sec III A 0 b, to be the resonance rabi frequency Δ_e addressing the nuclear configuration of $14N = +1$ and the carbons in up $+\frac{1}{2}$. The first line describes the coherent MW drive on the electronic qubit dependent on the nuclear configuration, while the second captures the weak, MW-mediated coupling pathway to nearby nuclear spins, only considering minor nuclear wobbles.

The specific physical parameters used in the simulation of the NV register are given in Appendix D.

B. Diagonal Three-Qubit Entangler

We apply the control framework based on support-selective phase invariants from Sec. II C to synthesize a diagonal three-qubit entangling gate. The target operation is

$$U_{\text{target}} = e^{i\frac{\pi}{4} Z \otimes Z \otimes Z}, \quad (30)$$

which generates a GHZ state up to local phases and thus produces genuine tripartite entanglement [63, 64].

As a concrete implementation, we simulate a solid-state register composed of an NV electronic spin (A) coupled to two proximal ^{13}C nuclear spins (B, C), with the ^{14}N nuclear spin prepared in a fixed m_I manifold acting as a spectator. Within the logical $A \otimes B \otimes C$ subspace, the goal is to realize a diagonal three-qubit gate whose interaction content consists exclusively of a three-body phase, while all pairwise couplings vanish. Residual single-qubit Z phases are corrected virtually using the corresponding first-order phase invariants.

Rather than targeting a fixed unitary matrix, the optimization objective is formulated directly in terms of desired phase interactions for the target unitary gate using corresponding phase invariants derived in Sec (II B). Using these phase invariants we optimize a control pulse

which steers the system toward a prescribed interaction-phase structure.

Since this target gate is already diagonal we do not require a diagonalizing frame first, and can, for this example, focus on the k -body resolution of interactions while using the explicit formulation given in Sec. (II C). In the canonical frame, the logical propagator takes the form

$$U_{\text{diag}} = \sum_{a,b,c \in \{0,1\}} e^{i\phi_{abc}} |abc\rangle \langle abc|, \quad (31)$$

from which the interaction phases are extracted via the S -phase invariants $\Delta_S(\phi)$ introduced in Secs. II B–II C. For a three-qubit system, the relevant phase invariants are

$$\Delta_{\{a\}}, \Delta_{\{b\}}, \Delta_{\{c\}}, \Delta_{\{a,b\}}, \Delta_{\{a,c\}}, \Delta_{\{b,c\}}, \Delta_{\{a,b,c\}}. \quad (32)$$

Explicit formulas for these phase invariants in terms of the experimentally accessible diagonal phase values $\{\phi_x\}_{x \in \{0,1\}^3}$ are given in Appendix B.

We note, that each phase invariant $\Delta_S(\phi)$ directly reveals the $|S|$ -body interaction phase associated with the qubit subset S , independent of all other contributions.

The control objective is therefore defined explicitly in phase invariant space by specifying the target values

$$\Delta_{\{a,b,c\}}^* = \frac{\pi}{4}, \quad \Delta_{\{a,b\}}^* = \Delta_{\{a,c\}}^* = \Delta_{\{b,c\}}^* = 0, \quad (33)$$

with no constraints imposed on the single-qubit phase invariants $\Delta_{\{a\}}, \Delta_{\{b\}}, \Delta_{\{c\}}$. The optimization then minimizes the π -periodic phase-map cost function \mathcal{J}_{3q} defined in Eq. (25), with weights chosen such that only nonlocal interactions ($|S| \geq 2$) contribute. This selectively drives the three-body interaction phase to its target value while suppressing all lower-order nonlocal phase contributions, up a to global phase. Additional regularization terms penalize leakage, non-unitarity, and rapid control variations. The resulting control pulse and induced many-body phase dynamics are illustrated in Figs. 1 and 2.

The optimized microwave envelope (Fig. 1) exhibits smooth amplitude and phase modulation over $T = 1500$ ns and realizes the desired diagonal-phase-map objective as a single shaped pulse.

For time-resolved validation, we evaluate the diagonal phase map throughout the driven evolution and track the induced phases via the phase invariants $\Delta_S(\phi(t))$ for all nonempty subsets $S \subseteq \{a, b, c\}$. This reveals directly how the control pulse builds up the desired three-body interaction phase $\Delta_{\{a,b,c\}}$ while suppressing the pairwise phase components $\Delta_{\{a,b\}}, \Delta_{\{a,c\}}, \Delta_{\{b,c\}}$ during the entire gate time, up to the inherent 2π -periodicity of the phase map. Fig. 2 shows the resulting phase invariant trajectories.

Residual single-qubit phases are removed via local Z corrections determined from the first-order phase invariants

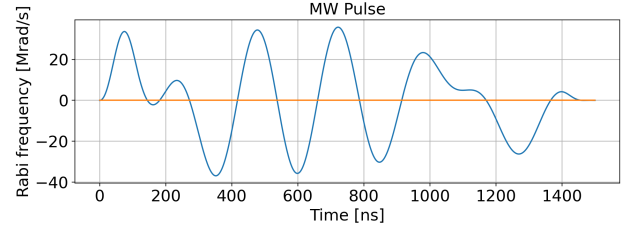


FIG. 1: Optimized microwave envelope realizing the diagonal phase-map control objective. The pulse selectively results in a finite three-body phase as given by the three-body phase invariant $\Delta_{\{a,b,c\}} \approx \pi/4$ modulo π , while suppressing all two-body phases as given by the two-body correlators $\Delta_{\{a,b\}}, \Delta_{\{a,c\}}, \Delta_{\{b,c\}}$ similarly.

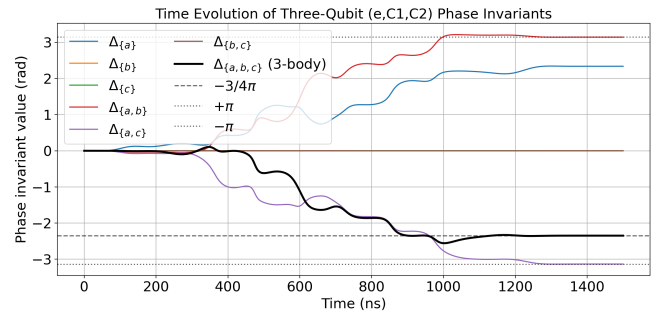


FIG. 2: Time evolution of the phase invariants $\Delta_S(\phi(t))$ extracted from the diagonal phase map of the logical three-qubit subspace during the optimized pulse. To probe all phases specified with the given set of phase invariants, we initialize the system in $|+\rangle$ states in the diagonalizing frame. The three-body phase invariant $\Delta_{\{a,b,c\}}$ (thick black line) converges to $-3\pi/4$, which is physically equivalent to the target value $\pi/4$ in entangling effect. The two-body phase invariants $\Delta_{\{a,b\}}, \Delta_{\{a,c\}},$ and $\Delta_{\{b,c\}}$ approach integer multiples of π , corresponding to vanishing pairwise interaction content. Single-qubit phase invariants $\Delta_{\{a\}}, \Delta_{\{b\}}, \Delta_{\{c\}}$ correspond to local Z phases.

$\Delta_{\{a\}}, \Delta_{\{b\}}, \Delta_{\{c\}}$, yielding the local correction operator

$$U_{\text{loc}} = \exp\left(-i2 \sum_{j \in \{a,b,c\}} \Delta_{\{j\}} Z_j\right), \quad (34)$$

which leaves all nonlocal phases unchanged and can usually be corrected via shifting the local phase references virtually. The effective operation

$$U_{\text{final}} = U_{\text{loc}} U_{\text{pulse}} \quad (35)$$

achieves a fidelity of

$$F_{\text{ZZZ}} = \frac{|\text{Tr}[(U_{\text{target}})^\dagger U_{\text{final}}]|^2}{8^2} = 0.9978 \quad (36)$$

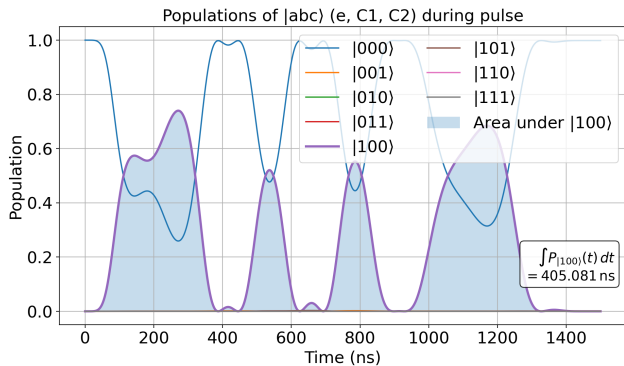


FIG. 3: Three-qubit population dynamics during the optimized control pulse for implementing the diagonal target gate $e^{i\frac{\pi}{4}Z\otimes Z\otimes Z}$. The shaded area indicates the time-integrated population of the decoherence-prone electronic $m_s = -1$ manifold used to estimate the accumulated dephasing.

with the ideal three-qubit entangler in Eq. (30).

Additionally, we roughly estimate possible decoherence effects using a time-integrated dephasing functional based on the exposure time of the electron in the $m_s = -1$ manifold,

$$\mathcal{D} = \exp\left[-\frac{1}{T_2} \int p_{-1}(t) dt\right], \quad (37)$$

where $p_{-1}(t)$ denotes the instantaneous population of the electronic $m_s = -1$ state along the control trajectory, which is particularly prone to decoherence due to hyperfine-induced splittings [49, 51], and T_2 is the corresponding electronic dephasing time. This functional provides a simple approximative measure of the accumulated dephasing during the gate, similarly done in [65].

The shaded area under the population trajectory shown in Fig. 3 provides the time-integrated exposure of the electron. Taking from this area an exposure of approximately $0.4 \mu\text{s}$ and assuming an electronic dephasing time in the range $T_2^* \sim 0.5\text{--}1 \text{ ms}$ [66, 67] yields

$$F_{ZZZ} \lesssim \mathcal{D} = \exp\left(-\frac{0.4 \mu\text{s}}{T_2^*}\right) \approx 0.9992\text{--}0.9996, \quad (38)$$

providing a rough upper-bound estimate of the achievable gate fidelity under electron-spin decoherence, for this particular realization.

This result shows how phase invariant based control objectives can be applied to synthesizing canonically diagonal three-qubit entanglers. In the following we will demonstrate the same for a naturally non-diagonal gate and discuss the multitude of benefits in the last section, after that.

C. Non-diagonal Three-Qubit Entangler

We now apply the phase invariants based control framework of Sec. II C to synthesize an example *non-diagonal* three-qubit entangling gate by performing the optimization in a diagonalizing frame. The target operation is

$$U_{\text{target}} = e^{i\frac{\pi}{4}X\otimes Z\otimes Z}, \quad (39)$$

which also generates a GHZ state up to local phases and thus produces genuine tripartite entanglement [63, 64]. This target gate is not naturally diagonal and will therefore serve as an explicit example for the usage of our framework, highlighting its functionality in a diagonal frame for arbitrary gates.

The optimization that induces this target gate is thus carried out in this *Hadamard-sandwiched frame*,

$$\begin{aligned} U_{\text{diag}} &= (H_A \otimes I_B \otimes I_C) U_{\text{pulse}} (H_A \otimes I_B \otimes I_C) \\ &= e^{i\frac{\pi}{4}Z\otimes Z\otimes Z}, \end{aligned} \quad (40)$$

where the target unitary is diagonal and can be analyzed directly using the phase invariant formalism of Secs. II B–II C. After optimization, the Hadamard gates are removed such that the same physical pulse implements the desired non-diagonal action in the computational basis.

As before, we simulate a solid-state register consisting of an NV electronic spin (A) coupled to two proximal ^{13}C nuclear spins (B, C), with the ^{14}N nuclear spin fixed in a spectator m_I manifold. Within the logical $A \otimes B \otimes C$ subspace, the optimization seeks a diagonal operation in the Hadamard frame whose interaction content consists of a finite three-body phase and vanishing pairwise couplings. Residual single-qubit Z phases are corrected virtually using the corresponding first-order phase invariants.

In the new diagonalized frame, the optimization proceeds as before, via Eqs. 31–33. The optimization target is again formulated based on the desired interaction phases via corresponding phase invariants. Explicit formulas for these k -body selective phase invariants in terms of the experimentally accessible diagonal phase values $\{\phi_x\}_{x \in \{0,1\}^3}$ are given in Appendix B. Using these phase invariants we optimize a control pulse which steers the system toward a prescribed interaction-phase structure.

After optimization in the diagonalizing frame, we return to the computational basis by discarding the Hadamard gates in Eq. (40), such that the effective action of the pulse is

$$U_{\text{pulse}} \approx e^{i\frac{\pi}{4}X\otimes Z\otimes Z}. \quad (41)$$

The resulting control pulse and induced dynamics are illustrated in Figs. 4 and 5. The optimized microwave envelope (Fig. 4) exhibits smooth amplitude and phase modulation

over $T = 1250$ ns and realizes the desired phase-map control objective in the diagonalizing (Hadamard) frame as a single shaped pulse. After the removal of the diagonalizing transformations, the same physical pulse implements the target non-diagonal entangler in the computational basis.

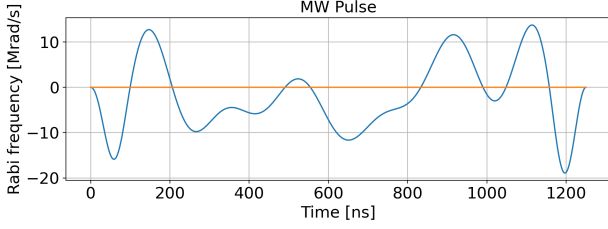


FIG. 4: Optimized microwave envelope implementing the non-diagonal three-qubit entangler $e^{i(\pi/4)X \otimes Z \otimes Z}$ in the computational basis, synthesized via phase invariant optimization in the diagonalizing (Hadamard) frame.

Next we analyse the time dependence of the dynamics, where we can use as a tool the diagonal phase map in the Hadamard frame throughout the driven evolution and track the induced phase invariants $\Delta_S(\phi(t))$ for all nonempty subsets $S \subseteq \{a, b, c\}$. This reveals directly how the control pulse builds up the desired three-body interaction phase $\Delta_{\{a,b,c\}}$ in the diagonalizing frame while suppressing the pairwise phase components $\Delta_{\{a,b\}}, \Delta_{\{a,c\}}, \Delta_{\{b,c\}}$ during the entire gate time, up to the inherent 2π -periodicity of the phase map. Figure 5 shows the resulting phase invariant trajectories.

Residual local phases are extracted via the first-order phase invariants in the diagonalizing frame and yield the local correction operator

$$U_{\text{loc}}^{(\text{diag})} = \exp\left(-i \sum_{j \in \{a,b,c\}} \Delta_{\{j\}} Z_j\right). \quad (42)$$

Transforming back to the computational basis gives

$$U_{\text{loc}}^{(\text{comp})} = (H_A \otimes I_B \otimes I_C) U_{\text{loc}}^{(\text{diag})} (H_A \otimes I_B \otimes I_C) = e^{i(\Delta_{\{a\}} X_A + \Delta_{\{b\}} Z_B + \Delta_{\{c\}} Z_C)}. \quad (43)$$

Note that here the local X rotation cannot be corrected virtually and an additional single-qubit gate is needed. The final operation is then

$$U_{\text{final}} = U_{\text{loc}}^{(\text{comp})} U_{\text{pulse}}. \quad (44)$$

The fidelity with the target operation in Eq. (39) evaluates to

$$F_{\text{XZZ}} = \frac{|\text{Tr}[(U_{\text{target}})^\dagger U_{\text{final}}]|^2}{8^2} = 0.9985, \quad (45)$$

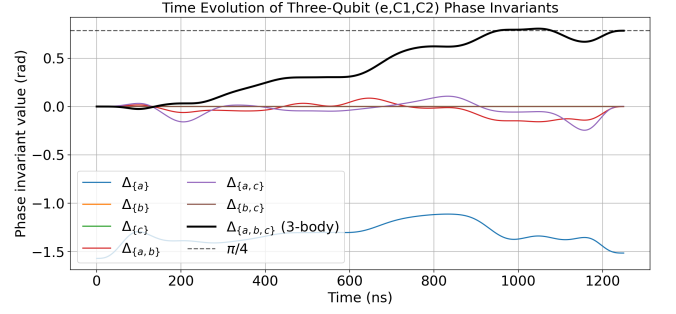


FIG. 5: Time evolution of the phase invariants $\Delta_S(\phi(t))$ extracted from the diagonal phase map in the diagonalizing (Hadamard) frame during the optimized non-diagonal gate pulse. To be able to probe all phases that we specified via phase invariants, we initialize the system in $|+\rangle$ states in the diagonalizing frame, corresponding to the computational-basis state $|0++\rangle$. As in Fig. 2, the three-body phase invariants $\Delta_{\{a,b,c\}}$ (thick black line) converges to $\pi/4$, realizing the desired three-body interaction, up to single-qubit phases, in the Hadamard frame. The two-body phase invariants $\Delta_{\{a,b\}}, \Delta_{\{a,c\}},$ and $\Delta_{\{b,c\}}$ approach values corresponding to vanishing pairwise interaction content.

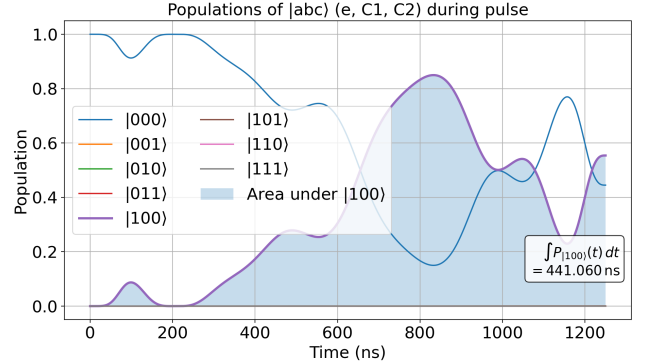


FIG. 6: Three-qubit population dynamics during the optimized control pulse for implementing the diagonal target gate $e^{i\frac{\pi}{4}X \otimes Z \otimes Z}$. The shaded area indicates the time-integrated population of the decoherence-prone electronic $m_s = -1$ manifold used to estimate the accumulated dephasing.

demonstrating that phase-map optimization in a diagonalizing frame extends naturally to high-fidelity non-diagonal multiqubit gates.

Additionally, we again approximately determine possible decoherence effects using a time-integrated dephasing functional based on the exposure time of the electron in the dephasing prone $m_s = -1$ manifold, see again equation (37).

The shaded area under the population trajectory shown in Fig. 6 provides the time-integrated exposure of the electron. Taking from this area an exposure of approximately $0.4 \mu\text{s}$ and assuming an electronic dephasing time in the range $T_2^* \sim 0.5\text{--}1 \text{ ms}$ [66, 67] yields

$$F_{XZZ} \lesssim \mathcal{D} = \exp\left(-\frac{0.45 \mu\text{s}}{T_2^*}\right) \approx 0.9991\text{--}0.9995, \quad (46)$$

providing a rough upper bound estimate for the achievable gate fidelity in the presence of electron-spin decoherence, for this particular realization.

These results show, how embedding the phase invariant based control objective frame does enable synthesis of non-diagonal three-qubit entanglers within an appropriate diagonal frame. The resulting pulse realizes a high-fidelity XZZ -type interaction, illustrating the generality and flexibility of the phase invariant based control framework. Such terms as the XZZ occur in stabilizer measurements, making this directly useful not only in entangled state preparation but also for QEC syndrome extraction [68–70].

IV. CONCLUSION AND OUTLOOK

We introduced a k -body-resolved interaction decomposition of the diagonal phase map that enables general multi-qubit control objectives to be formulated in a diagonal frame, thereby enabling to optimize controls for n -qubit unitary transformation in a diagonal frame during the optimization. This reduces characterization costs quadratically with qubit number and improves scalability significantly. For that, we showed analytically how to construct phase invariants that deterministically isolate and quantify any k -body interactions which are encoded as phase contributions in the diagonal phase map of the unitary transformation. Because the derived phase invariants exist for all subsets $S \subseteq \{1, \dots, n\}$, this formulation extends directly to arbitrary n -qubit (gate) transformations and arbitrary k -body interactions. These deterministic phase invariants form a mathematically self-contained coordinate system on the diagonal phase map and give rise to compact, differentiable control, and interaction-resolved objectives, which also allows to omit specifying irrelevant interactions terms, thereby avoiding over-constraining the optimization. The lower characterization cost together with reduced optimization overhead makes this framework an advantageous candidate for the closed-loop synthesis of complex multi-qubit gates.

To illustrate the framework, we synthesized two distinct *genuinely three-partite entangling* operations, each implemented as a single shaped microwave pulse, in a simulated realistic $\text{NV}^{-14}\text{N}^{-13}\text{C}^{-13}\text{C}$ register. First, we generated optimal controls for a *diagonal* $e^{i(\pi/4)Z \otimes Z \otimes Z}$ gate whose nonzero three-body phase cannot be reduced

to pairwise interactions, achieving a overlap fidelity of $F_{ZZZ} = 0.9978$. This serves as an application example for a naturally diagonal gate transformation. Second, we generated optimal controls for a *non-diagonal* $e^{i(\pi/4)X \otimes Z \otimes Z}$ entangler by optimizing in a diagonalizing (Hadamard-sandwiched) frame and transforming back to the computational basis, reaching $F_{XZZ} = 0.9985$. This serves as an application example for a naturally non-diagonal gate transformation being considered in a diagonalizing frame during the control optimization. In both cases, all residual single-qubit phases were corrected using virtual local operations derived from the same phase invariant hierarchy. These results demonstrate that diagonal-phase-map objectives naturally support the efficient synthesis of truly multipartite entangling gates.

Beyond their intrinsic control-theoretic interest, our numerical experiments also demonstrate the ability to synthesize higher-weight multi-qubit interactions in a single microwave pulse on NV center spin registers, which has direct implications for achieving multi-qubit entanglement and quantum error correction on these, and similar AMO systems. Conventionally, achieving multi-qubit entanglement typically relies on decomposing the desired interaction into a sequences of sub-pulses and into sequences of two-qubit gates [52–54, 71]. Many stabilizer measurements require effective three- or four-body parity checks, which are typically decomposed into sequences of two-qubit entanglers and ancilla-mediated gates [68–70, 72]. These conventional approaches lead to operation times in the range of tens to hundreds of microseconds in NV center spin registers [52–54, 71]. In contrast, our shaped-pulse synthesis produces the full tripartite entanglement in single microwave pulses of only $1.25\mu\text{s}$ and $1.5\mu\text{s}$, representing a factor 10-100 reduction in operation time compared with the fastest existing NV-based multi-qubit entanglers that act on more than two qubits at once [52–54]. Access to such short-duration single shot pulses reduces circuit depth, minimizes ancilla exposure, and suppresses error accumulation, thereby improving the overall robustness and speed of protocols. With NV electron-spin coherence times ranging from $\sim 0.5\text{--}1 \text{ ms}$ at room temperature [66, 67] and extending to several milliseconds under dynamical decoupling in multi-qubit registers [72], these coherence windows allow a ratio of $5 \cdot 10^{-3}\text{--}10^{-4}$ between our $1.25\text{--}1.5 \mu\text{s}$ gate duration and the available coherence time. And beyond quantum error correction, such compact multi-spin control may also benefit quantum-simulation platforms, where only specific k -body terms of an effective Hamiltonian need to be engineered or calibrated. Efficient access to many-body interactions in a single shot is directly relevant to programmable quantum simulators based on Rydberg and neutral-atom arrays [73–76], which routinely rely on Ising-type couplings, multi-body gates.

Looking ahead, promising directions include closed-loop refinement using support-selective phase invariant based feedback estimators, robustness-aware optimization un-

der drift and control noise, and experimental realization on multi-spin NV centers and other AMO systems with electron-nuclear interactions. Altogether, phase-map based control objectives provide a more scalable and ex-

perimentally practical route to fast, high-fidelity synthesis of unitary multi-qubit gates, including genuinely multipartite entanglers, across diverse quantum architectures.

-
- [1] Christiane P Koch, Ugo Boscain, Tommaso Calarco, Gunther Dirr, Stefan Filipp, Steffen J Glaser, Ronnie Kosloff, Simone Montangero, Thomas Schulte-Herbrüggen, Dominique Sugny, et al. Quantum optimal control in quantum technologies. strategic report on current status, visions and goals for research in europe. *EPJ Quantum Technology*, 9(1):19, 2022.
- [2] Simon J Evered, Dolev Bluvstein, Marcin Kalinowski, Sepehr Ebadi, Tom Manovitz, Hengyun Zhou, Sophie H Li, Alexandra A Geim, Tout T Wang, Nishad Maskara, et al. High-fidelity parallel entangling gates on a neutral-atom quantum computer. *Nature*, 622(7982):268–272, 2023.
- [3] Yang Dong, Wang Jiang, Xue-Dong Gao, Cui Yu, Yong Liu, Shao-Chun Zhang, Xiang-Dong Chen, Ibério de PR Moreira, Josep Maria Bofill, Gael Sentís, et al. Time-optimal control of a solid-state spin amidst dynamical quantum wind. *npj Quantum Information*, 10(1):108, 2024.
- [4] Thomas Monz, Philipp Schindler, Julio T Barreiro, Michael Chwalla, Daniel Nigg, William A Coish, Maximilian Harlander, Wolfgang Hänsel, Markus Hennrich, and Rainer Blatt. 14-qubit entanglement: Creation and coherence. *Physical Review Letters*, 106(13):130506, 2011.
- [5] Harry Levine, Alexander Keesling, Giulia Semeghini, Ahmed Omran, Tout T Wang, Sepehr Ebadi, Hannes Bernien, Markus Greiner, Vladan Vuletić, Hannes Pichler, et al. Parallel implementation of high-fidelity multi-qubit gates with neutral atoms. *Physical review letters*, 123(17):170503, 2019.
- [6] Ahmed Omran, Harry Levine, Alexander Keesling, Giulia Semeghini, Tout T Wang, Sepehr Ebadi, Hannes Bernien, Alexander S Zibrov, Hannes Pichler, Soonwon Choi, et al. Generation and manipulation of schrödinger cat states in rydberg atom arrays. *Science*, 365(6453):570–574, 2019.
- [7] Xiao-Le Li, Ziyu Tao, Kangyuan Yi, Kai Luo, Libo Zhang, Yuxuan Zhou, Song Liu, Tongxing Yan, Yuanzhen Chen, and Dapeng Yu. Hardware-efficient and fast three-qubit gate in superconducting quantum circuits. *Frontiers of Physics*, 19(5):51205, 2024.
- [8] Kui Zhao, Wei-Guo Ma, Ziting Wang, Hao Li, Kaixuan Huang, Yun-Hao Shi, Kai Xu, and Heng Fan. Microwave-activated high-fidelity three-qubit gate scheme for fixed-frequency superconducting qubits. *Physical Review Applied*, 24(3):034064, 2025.
- [9] Edwin Barnes, Christian Arenz, Alexander Pitchford, and Sophia E Economou. Fast microwave-driven three-qubit gates for cavity-coupled superconducting qubits. *Physical Review B*, 96(2):024504, 2017.
- [10] Boxi Li, Tommaso Calarco, and Felix Motzoi. Experimental error suppression in cross-resonance gates via multi-derivative pulse shaping. *npj Quantum Information*, 10(1):66, 2024.
- [11] Y Gao, A Galicia, JD Jesus, Y Liu, Y Haddad, DA Volkov, JR Guimarães, H Bhardwaj, M Jerger, M Neis, et al. Ultrafast single qubit gates through multi-photon transition removal. *arXiv preprint arXiv:2511.22365*, 2025.
- [12] Yi Chou, Shang-Yu Huang, and Hsi-Sheng Goan. Optimal control of fast and high-fidelity quantum gates with electron and nuclear spins of a nitrogen-vacancy center in diamond. *Phys. Rev. A*, 91:052315, May 2015.
- [13] Matthew D. Grace, Constantin Brif, Herschel Rabitz, Daniel A. Lidar, Ian A. Walmsley, and Robert L. Kosut. Fidelity of optimally controlled quantum gates with randomly coupled multiparticle environments. *Journal of Modern Optics*, 54(16-17):2339–2349, 2007.
- [14] Frédéric Sauvage and Florian Mintert. Optimal control of families of quantum gates. *Physical review letters*, 129(5):050507, 2022.
- [15] Yaqing X Wang, Tommaso Calarco, Felix Motzoi, and Matthias M Müller. Circuit design for a star-shaped spin-qubit processor via algebraic decomposition and optimal control. *arXiv preprint arXiv:2506.16900*, 2025.
- [16] Navin Khaneja, Timo Reiss, Cindie Kehlet, Thomas Schulte-Herbrüggen, and Steffen J Glaser. Optimal control of coupled spin dynamics: design of nmr pulse sequences by gradient ascent algorithms. *Journal of magnetic resonance*, 172(2):296–305, 2005.
- [17] Pierre de Fouquieres, Sophie G Schirmer, Steffen J Glaser, and Ilya Kuprov. Second order gradient ascent pulse engineering. *Journal of Magnetic Resonance*, 212(2):412–417, 2011.
- [18] F Motzoi, Jay M Gambetta, Seth T Merkel, and Frank K Wilhelm. Optimal control methods for rapidly time-varying hamiltonians. *Physical Review A—Atomic, Molecular, and Optical Physics*, 84(2):022307, 2011.
- [19] Hannah J Hogben, Matthew Krzystyniak, Gareth TP Charnock, Peter J Hore, and Ilya Kuprov. Spinach—a software library for simulation of spin dynamics in large spin systems. *Journal of magnetic resonance*, 208(2):179–194, 2011.
- [20] Michael Goerz, Daniel Basilewitsch, Fernando Gago-Encinas, Matthias G Krauss, Karl P Horn, Daniel M Reich, and Christiane Koch. Krotov: A python implementation of krotov’s method for quantum optimal control. *SciPost physics*, 7(6):080, 2019.
- [21] Daniel M Reich, Mamadou Ndong, and Christiane P Koch. Monotonically convergent optimization in quantum control using krotov’s method. *The Journal of chemical physics*, 136(10), 2012.
- [22] Michael H Goerz, Daniel M Reich, and Christiane P Koch. Optimal control theory for a unitary operation under dissipative evolution. *New Journal of Physics*, 16(5):055012, 2014.
- [23] Tommaso Caneva, Tommaso Calarco, and Simone Montangero. Chopped random-basis quantum optimization. *Physical Review A—Atomic, Molecular, and Optical Physics*, 84(2):022326, 2011.
- [24] Niklas Rach, Matthias M Müller, Tommaso Calarco, and Simone Montangero. Dressing the chopped-random-basis

- optimization: A bandwidth-limited access to the trap-free landscape. *Physical Review A*, 92(6):062343, 2015.
- [25] Patrick Doria, Tommaso Calarco, and Simone Montangero. Optimal control technique for many-body quantum dynamics. *Physical review letters*, 106(19):190501, 2011.
- [26] Matthias Mueller, Ressa Suhardiman Said, Fedor Jelezko, Tommaso Calarco, and Simone Montangero. One decade of quantum optimal control in the chopped random basis. *Reports on Progress in Physics*, 2022.
- [27] Steffen J Glaser, Ugo Boscain, Tommaso Calarco, Christiane P Koch, Walter Köckenberger, Ronnie Kosloff, Ilya Kuprov, Burkhard Luy, Sophie Schirmer, Thomas Schulte-Herbrüggen, et al. Training schrödinger’s cat: Quantum optimal control: Strategic report on current status, visions and goals for research in europe. *The European Physical Journal D*, 69(12):279, 2015.
- [28] Francesco Preti, Tommaso Calarco, and Felix Motzoi. Continuous quantum gate sets and pulse-class meta-optimization. *PRX Quantum*, 3(4):040311, 2022.
- [29] José P Palao, Daniel M Reich, and Christiane P Koch. Steering the optimization pathway in the control landscape using constraints. *Physical Review A—Atomic, Molecular, and Optical Physics*, 88(5):053409, 2013.
- [30] Constantin Brif, Raj Chakrabarti, and Herschel Rabitz. Control of quantum phenomena: past, present and future. *New Journal of Physics*, 12(7):075008, 2010.
- [31] Jun Zhang, Jiri Vala, Shankar Sastry, and K Birgitta Whaley. Geometric theory of nonlocal two-qubit operations. *Physical Review A*, 67(4):042313, 2003.
- [32] LS Theis, F Motzoi, S Machnes, and FK Wilhelm. Counteracting systems of diabaticities using drag controls: The status after 10 years (a). *Europhysics Letters*, 123(6):60001, 2018.
- [33] David Guéry-Odelin, Andreas Ruschhaupt, Anthony Kiely, Erik Torrontegui, Sofia Martínez-Garaot, and Juan Gonzalo Muga. Shortcuts to adiabaticity: Concepts, methods, and applications. *Reviews of Modern Physics*, 91(4):045001, 2019.
- [34] Martino Calzavara, Tommaso Calarco, and Felix Motzoi. Classical feature map surrogates and metrics for quantum control landscapes. *arXiv preprint arXiv:2509.25930*, 2025.
- [35] Marcus Cramer, Martin B Plenio, Steven T Flammia, Rolando Somma, David Gross, Stephen D Bartlett, Olivier Landon-Cardinal, David Poulin, and Yi-Kai Liu. Efficient quantum state tomography. *Nature communications*, 1(1):149, 2010.
- [36] IA Luchnikov, MA Gavreev, and AK Fedorov. Controlling quantum many-body systems using reduced-order modeling. *Physical Review Research*, 6(1):013161, 2024.
- [37] Ariel Bendersky, Fernando Pastawski, and Juan Pablo Paz. Selective and efficient estimation of parameters for quantum process tomography. *Physical review letters*, 100(19):190403, 2008.
- [38] Sreeram PG and Vaibhav Madhok. Quantum tomography with random diagonal unitary maps and statistical bounds on information generation using random matrix theory. *Physical Review A*, 104(3), September 2021.
- [39] Xiaohua Wu and Ke Xu. Partial standard quantum process tomography. *Quantum information processing*, 12(2):1379–1393, 2013.
- [40] Gang-Qin Liu, Yu-Ran Zhang, Yan-Chun Chang, Jie-Dong Yue, Heng Fan, and Xin-Yu Pan. Demonstration of entanglement-enhanced phase estimation in solid. *Nature Communications*, 6(1):6726, 2015.
- [41] Michael A Nielsen and Isaac L Chuang. Quantum computation and quantum information. *Phys. Today*, 54(2):60, 2001.
- [42] Domenico d’Alessandro. *Introduction to quantum control and dynamics*. Chapman and hall/CRC, 2021.
- [43] Ryan O’Donnell. *Analysis of boolean functions*. Cambridge University Press, 2014.
- [44] Jonathan Welch, Daniel Greenbaum, Sarah Mostame, and Alan Aspuru-Guzik. Efficient quantum circuits for diagonal unitaries without ancillas. *New Journal of Physics*, 16(3):033040, 2014.
- [45] Audrey Terras. *Fourier Analysis on Finite Groups and Applications*, volume 43 of *London Mathematical Society Student Texts*. Cambridge University Press, Cambridge, 1999.
- [46] Paul Watts, Jiří Vala, Matthias M Müller, Tommaso Calarco, K Birgitta Whaley, Daniel M Reich, Michael H Goerz, and Christiane P Koch. Optimizing for an arbitrary perfect entangler. i. functionals. *Physical Review A*, 91(6):062306, 2015.
- [47] Michael H Goerz, Giulia Gualdi, Daniel M Reich, Christiane P Koch, Felix Motzoi, K Birgitta Whaley, Jiří Vala, Matthias M Müller, Simone Montangero, and Tommaso Calarco. Optimizing for an arbitrary perfect entangler. ii. application. *Physical Review A*, 91(6):062307, 2015.
- [48] AT Rezakhani. Characterization of two-qubit perfect entanglers. *Physical Review A—Atomic, Molecular, and Optical Physics*, 70(5):052313, 2004.
- [49] Romana Schirhagl, Kevin Chang, Michael Loretz, and Christian L. Degen. Nitrogen-vacancy centers in diamond: Nanoscale sensors for physics and biology. *Annual Review of Physical Chemistry*, 65(1):83–105, 2014. PMID: 24274702.
- [50] Philipp Neumann. *Towards a Room Temperature Solid State Quantum Processor – The Nitrogen-Vacancy Center in Diamond*. PhD thesis, Universität Stuttgart, 2012. PhD thesis.
- [51] YunHeng Chen, Sophie Stearn, Scott Vella, Andrew Horsley, and Marcus W Doherty. Optimisation of diamond quantum processors. *New Journal of Physics*, 22(9):093068, sep 2020.
- [52] Conor E Bradley, Joe Randall, Mohamed H Abobeih, Remon C Berrevoets, Maarten J Degen, Michiel A Bakker, Matthew Markham, Daniel J Twitchen, and Tim H Taminiau. A ten-qubit solid-state spin register with quantum memory up to one minute. *Physical Review X*, 9(3):031045, 2019.
- [53] Joseph D Minnella, Mathieu Ouellet, Amelia R Klein, and Lee C Bassett. Single-gate, multipartite entanglement on a room-temperature quantum register. *arXiv preprint arXiv:2508.08465*, 2025.
- [54] Evangelia Takou, Edwin Barnes, and Sophia E Economou. Generation of genuine all-way entanglement in defect-nuclear spin systems through dynamical decoupling sequences. *Quantum*, 8:1304, 2024.
- [55] Marcus W. Doherty, Chunhui Rita Du, and Gregory D. Fuchs. Quantum science and technology based on color centers with accessible spin. *Journal of Applied Physics*, 131(1):010401, 2022.
- [56] Thomas K Unden, Daniel Louzon, Michael Zwolak, Wojciech Hubert Zurek, and Fedor Jelezko. Revealing the emergence of classicality using nitrogen-vacancy centers.

- Physical review letters*, 123(14):140402, 2019.
- [57] Oleg V Morzhin and Alexander N Pechen. Krotov method for optimal control of closed quantum systems. *Russian Mathematical Surveys*, 74(5):851, 2019.
- [58] Niels E. Henriksen. Laser control of chemical reactions. *Chem. Soc. Rev.*, 31:37–42, 2002.
- [59] Sebastian Deffner and Eric Lutz. Quantum speed limit for non-markovian dynamics. *Physical review letters*, 111(1):010402, 2013.
- [60] Kamal Bhattacharyya. Quantum decay and the mandelstam-tamm-energy inequality. *Journal of Physics A: Mathematical and General*, 16(13):2993, 1983.
- [61] JJWH Sorensen, MO Aranburu, T Heinzl, and JF Sherson. Quantum optimal control in a chopped basis: Applications in control of bose-einstein condensates. *Physical Review A*, 98(2):022119, 2018.
- [62] Jens Jakob Sørensen, Jacob Søgaard Nyemann, Felix Motzoi, Jacob Sherson, and Thomas Vosegaard. Optimization of pulses with low bandwidth for improved excitation of multiple-quantum coherences in nmr of quadrupolar nuclei. *The Journal of Chemical Physics*, 152(5), 2020.
- [63] Valerie Coffman, Joydip Kundu, and William K Wootters. Distributed entanglement. *Physical Review A*, 61(5):052306, 2000.
- [64] Wolfgang Dür, Guifre Vidal, and J Ignacio Cirac. Three qubits can be entangled in two inequivalent ways. *Physical Review A*, 62(6):062314, 2000.
- [65] Nicolas Roch, Mollie E Schwartz, Felix Motzoi, Christopher Macklin, Rajamani Vijay, Andrew W Eddins, Alexander N Korotkov, K Birgitta Whaley, Mohan Sarovar, and Irfan Siddiqi. Observation of measurement-induced entanglement and quantum trajectories of remote superconducting qubits. *Physical review letters*, 112(17):170501, 2014.
- [66] Gopalakrishnan Balasubramanian, Philipp Neumann, Daniel Twitchen, Matthew Markham, Roman Kolesov, Norikazu Mizuochi, Junichi Isoya, Jocelyn Achard, Johannes Beck, Julia Tissler, et al. Ultralong spin coherence time in isotopically engineered diamond. *Nature materials*, 8(5):383–387, 2009.
- [67] Peter Christian Maurer, Georg Kucsko, Christian Latta, Liang Jiang, Norman Ying Yao, Steven D Bennett, Fernando Pastawski, David Hunger, Nicholas Chisholm, Matthew Markham, et al. Room-temperature quantum bit memory exceeding one second. *Science*, 336(6086):1283–1286, 2012.
- [68] Daniel Gottesman. *Stabilizer codes and quantum error correction*. California Institute of Technology, 1997.
- [69] Austin G Fowler, Matteo Mariantoni, John M Martinis, and Andrew N Cleland. Surface codes: Towards practical large-scale quantum computation. *Physical Review A—Atomic, Molecular, and Optical Physics*, 86(3):032324, 2012.
- [70] Daniel Litinski. A game of surface codes: Large-scale quantum computing with lattice surgery. *Quantum*, 3:128, 2019.
- [71] HB Van Ommen, GL Van De Stolpe, N Demetriou, HKC Beukers, Jiwon Yun, TRJ Fortuin, M Iuliano, AR-P Montblanch, R Hanson, and TH Taminiau. Improved electron-nuclear quantum gates for spin sensing and control. *PRX Quantum*, 6(2):020309, 2025.
- [72] Tim Hugo Taminiau, Julia Cramer, Toeno van der Sar, Viatcheslav V Dobrovitski, and Ronald Hanson. Universal control and error correction in multi-qubit spin registers in diamond. *Nature nanotechnology*, 9(3):171–176, 2014.
- [73] Minh-Thi Nguyen, Jin-Guo Liu, Jonathan Wurtz, Mikhail D Lukin, Sheng-Tao Wang, and Hannes Pichler. Quantum optimization with arbitrary connectivity using rydberg atom arrays. *PRX Quantum*, 4(1):010316, 2023.
- [74] Daniel González-Cuadra, Dolev Bluvstein, Marcin Kalinowski, Raphael Kaubruegger, Nishad Maskara, Piero Naldesi, Torsten V Zache, Adam M Kaufman, Mikhail D Lukin, Hannes Pichler, et al. Fermionic quantum processing with programmable neutral atom arrays. *Proceedings of the National Academy of Sciences*, 120(35):e2304294120, 2023.
- [75] Dolev Bluvstein, Ahmed Omran, Harry Levine, Alexander Keesling, Giulia Semeghini, Sepehr Ebad, Tout T Wang, Alexios A Michailidis, Nishad Maskara, Wen Wei Ho, et al. Controlling quantum many-body dynamics in driven rydberg atom arrays. *Science*, 371(6536):1355–1359, 2021.
- [76] Iris Cong, Harry Levine, Alexander Keesling, Dolev Bluvstein, Sheng-Tao Wang, and Mikhail D Lukin. Hardware-efficient, fault-tolerant quantum computation with rydberg atoms. *Physical Review X*, 12(2):021049, 2022.
- [77] Bora Baran. Towards scalable multi-qubit optimal control via interaction decomposition in the diagonal frame. <https://doi.org/10.5281/zenodo.18714747>, 2026. Zenodo, Version v1.0.2. Software.
- [78] Arthur Schweiger and Gunnar Jeschke. *Principles of pulse electron paramagnetic resonance*. Oxford university press, 2001.
- [79] A P Nizovtsev, S Ya Kilin, A L Pushkarchuk, V A Pushkarchuk, and F Jelezko. Theoretical study of hyperfine interactions and optically detected magnetic resonance spectra by simulation of the c291[nv]-h172 diamond cluster hosting nitrogen-vacancy center. *New Journal of Physics*, 16(8):083014, aug 2014.

AUTHOR CONTRIBUTIONS

The project originated from discussions among all authors concerning the constructability of higher-order versions of local invariants. B.B. derived the generalization as support-selective phase invariants on the diagonal phase map and incorporated it into a control framework. M.M.M. and F.M. supervised the project. T.C., M.M.M. and F.M. provided scientific guidance and critical analysis throughout its development. B.B. drafted the manuscript and performed the numerical demonstration. All authors contributed to, reviewed and approved the final manuscript.

ACKNOWLEDGEMENTS

The authors acknowledge fruitful discussions with T. Reisser and M. Doherty regarding the and NV-Hamiltonian. This work was supported by the European Union’s HORIZON Europe program via project SPINUS (No. 101135699), project QCFD (101080085, HORIZON-CL4-2021 DIGITAL-EMERGING02-10), project OpenSuperQ-Plus100 (101113946, HORIZON-

CL4-2022-QUANTUM-01-SGA), by AIDAS-AI, Data Analytics and Scalable Simulation, which is a Joint Virtual Laboratory gathering the Forschungszentrum Juelich and the French Alternative Energies and Atomic Energy Commission, and by Germany's Excellence Strategy - the Cluster of Excellence Matter and Light for Quantum Computing (ML4Q2) EXC 2004/2 - 390534769.

DATA AVAILABILITY

The data and reproduction code is openly available on Zenodo and GitHub [77].

Appendix A: Alternating-sum Identity of Phase Invariants

Lemma 1 (Alternating-sum Identity of phase invariants). *Let $\phi : \{0,1\}^n \rightarrow \mathbb{R}/2\pi\mathbb{Z}$ be the phase map introduced in Section II A, and let δ_i denote the normalized discrete derivative defined in (11). For any nonempty subset $S \subseteq \{1, \dots, n\}$ define $\delta_S := \prod_{i \in S} \delta_i$ and*

$$\Delta_S(\phi) = \frac{1}{2^{|\bar{S}|}} \sum_{x_{\bar{S}} \in \{0,1\}^{\bar{S}}} (\delta_S \phi)(x_S, x_{\bar{S}}). \quad (\text{A1})$$

Then $\Delta_S(\phi)$ admits the alternating-sum identity

$$\Delta_S(\phi) = \frac{(-1)^{|S|}}{2^n} \sum_{x \in \{0,1\}^n} (-1)^{\sum_{i \in S} x_i} \phi(x). \quad (\text{A2})$$

Proof. We first prove the alternating-sum identity for the multi-variable discrete derivative: for any nonempty subset $S \subseteq \{1, \dots, n\}$,

$$(\delta_S \phi)(0) = \frac{(-1)^{|S|}}{2^{|S|}} \sum_{x_S \in \{0,1\}^S} (-1)^{\sum_{i \in S} x_i} \phi(x_S, 0_{\bar{S}}), \quad (\text{A3})$$

where only the coordinates in S are varied and all coordinates in \bar{S} are fixed at 0. The proof is by induction on $|S|$.

Base case ($|S| = 1$). Let $S = \{i\}$. Then

$$\begin{aligned} (\delta_i \phi)(0) &= \frac{1}{2} [\phi(1_i, 0_{\bar{S}}) - \phi(0_i, 0_{\bar{S}})] \\ &= -\frac{1}{2} \sum_{x_i \in \{0,1\}} (-1)^{x_i} \phi(x_i, 0_{\bar{S}}), \end{aligned} \quad (\text{A4})$$

which agrees with (A3) for $|S| = 1$.

Induction step. Let S be of size $k \geq 2$, and write

$$S = S' \cup \{j\}, \quad |S'| = k - 1. \quad (\text{A5})$$

Assume the statement holds for S' , i.e.

$$(\delta_{S'} \phi)(0) = \frac{(-1)^{k-1}}{2^{k-1}} \sum_{x_{S'}} (-1)^{\sum_{i \in S'} x_i} \phi(x_{S'}, 0_{\bar{S}'}). \quad (\text{A6})$$

Define $f := \delta_{S'} \phi$. Then

$$(\delta_j f)(0) = \frac{1}{2} [f(1_j) - f(0_j)]. \quad (\text{A7})$$

Using the induction hypothesis with the j -th coordinate fixed,

$$\begin{aligned} f(z_j) &= \frac{(-1)^{k-1}}{2^{k-1}} \sum_{x_{S'}} (-1)^{\sum_{i \in S'} x_i} \phi(x_{S'}, z_j, 0_{\bar{S}}), \\ z_j &\in \{0,1\}. \end{aligned} \quad (\text{A8})$$

Therefore,

$$\begin{aligned} (\delta_j f)(0) &= \frac{(-1)^{k-1}}{2^k} \sum_{x_{S'}} (-1)^{\sum_{i \in S'} x_i} \left[\phi(x_{S'}, 1_j, 0_{\bar{S}}) - \phi(x_{S'}, 0_j, 0_{\bar{S}}) \right] \\ &= \frac{(-1)^k}{2^k} \sum_{x_{S'}, x_j} (-1)^{\sum_{i \in S'} x_i + x_j} \phi(x_{S'}, x_j, 0_{\bar{S}}), \end{aligned}$$

here we recognize this as the two-term alternating sum in x_j . Since $\delta_S = \delta_j \delta_{S'}$, this yields

$$(\delta_S \phi)(0) = \frac{(-1)^k}{2^k} \sum_{x_S} (-1)^{\sum_{i \in S} x_i} \phi(x_S, 0_{\bar{S}}), \quad (\text{A9})$$

which is precisely (A3).

We now derive the phase invariant's alternating-sum identity. By definition,

$$\Delta_S(\phi) = \frac{1}{2^{|\bar{S}|}} \sum_{x_{\bar{S}} \in \{0,1\}^{\bar{S}}} (\delta_S \phi)(x_S, x_{\bar{S}}). \quad (\text{A10})$$

For each fixed $x_{\bar{S}}$, applying (A3) to the function $x_S \mapsto \phi(x_S, x_{\bar{S}})$ gives

$$(\delta_S \phi)(x_S, x_{\bar{S}}) = \frac{(-1)^{|S|}}{2^{|S|}} \sum_{x_S \in \{0,1\}^S} (-1)^{\sum_{i \in S} x_i} \phi(x_S, x_{\bar{S}}). \quad (\text{A11})$$

Substituting this into the definition of $\Delta_S(\phi)$ and combining the sums over x_S and $x_{\bar{S}}$ yields

$$\begin{aligned} \Delta_S(\phi) &= \frac{(-1)^{|S|}}{2^{|\bar{S}|+|S|}} \sum_{x_S, x_{\bar{S}}} (-1)^{\sum_{i \in S} x_i} \phi(x_S, x_{\bar{S}}) \\ &= \frac{(-1)^{|S|}}{2^n} \sum_{x \in \{0,1\}^n} (-1)^{\sum_{i \in S} x_i} \phi(x), \end{aligned} \quad (\text{A12})$$

which is (A2). \square

Appendix B: Explicit Three-Qubit Phase Invariants

The phase invariants $\Delta_S(\phi)$ were defined and derived in Section II B as exact support filters for the diagonal phase map. An explicit alternating-sum representation of these phase invariants was established in Appendix A. For the three-qubit case, this representation yields closed-form expressions directly in terms of the diagonal phase data $\{\phi_{000}, \dots, \phi_{111}\}$.

Specializing Eq. (A2) to $n = 3$, the support- S phase invariant takes the form

$$\Delta_S(\phi) = \frac{(-1)^{|S|}}{8} \sum_{a,b,c \in \{0,1\}} (-1)^{\sum_{i \in S} x_i} \phi_{abc}, \quad (\text{B1})$$

where $x = (a, b, c)$ and $S \subseteq \{a, b, c\}$. The explicit expressions for all nontrivial subsets S are listed below.

Three-body correlator $\Delta_{\{a,b,c\}}$. The support- $\{a, b, c\}$ interaction is

$$\Delta_{\{a,b,c\}}(\phi) = \frac{1}{8} \sum_{a,b,c} (-1)^{a+b+c} \phi_{abc}. \quad (\text{B2})$$

Explicitly,

$$\Delta_{\{a,b,c\}} = \frac{1}{8} \left(\phi_{000} - \phi_{001} - \phi_{010} + \phi_{011} - \phi_{100} + \phi_{101} + \phi_{110} - \phi_{111} \right) \quad (\text{B3})$$

Two-body correlators. For the pair $\{a, b\}$, we have

$$\Delta_{\{a,b\}}(\phi) = \frac{1}{8} \sum_{a,b,c} (-1)^{a+b} \phi_{abc}, \quad (\text{B4})$$

which gives

$$\Delta_{\{a,b\}} = \frac{1}{8} \left(\phi_{000} + \phi_{001} - \phi_{010} - \phi_{011} - \phi_{100} - \phi_{101} + \phi_{110} + \phi_{111} \right) \quad (\text{B5})$$

By symmetry,

$$\Delta_{\{a,c\}} = \frac{1}{8} \left(\phi_{000} - \phi_{001} + \phi_{010} - \phi_{011} - \phi_{100} + \phi_{101} - \phi_{110} + \phi_{111} \right) \quad (\text{B6})$$

and

$$\Delta_{\{b,c\}} = \frac{1}{8} \left(\phi_{000} - \phi_{001} - \phi_{010} + \phi_{011} + \phi_{100} - \phi_{101} - \phi_{110} + \phi_{111} \right) \quad (\text{B7})$$

Single-qubit correlators. For qubit a ,

$$\Delta_{\{a\}}(\phi) = \frac{1}{8} \sum_{a,b,c} (-1)^a \phi_{abc}, \quad (\text{B8})$$

so

$$\Delta_{\{a\}} = \frac{1}{8} \left(\phi_{000} + \phi_{001} + \phi_{010} + \phi_{011} - \phi_{100} - \phi_{101} - \phi_{110} - \phi_{111} \right) \quad (\text{B9})$$

Similarly,

$$\Delta_{\{b\}} = \frac{1}{8} \left(\phi_{000} + \phi_{001} - \phi_{010} - \phi_{011} + \phi_{100} + \phi_{101} - \phi_{110} - \phi_{111} \right) \quad (\text{B10})$$

$$\Delta_{\{c\}} = \frac{1}{8} \left(\phi_{000} - \phi_{001} + \phi_{010} - \phi_{011} + \phi_{100} - \phi_{101} + \phi_{110} - \phi_{111} \right) \quad (\text{B11})$$

Appendix C: Full Derivation of the NV-Center Hamiltonian

This appendix details the derivation of the effective NV-center Hamiltonian summarized in Sec. III A. The final expression corresponds to the working model used throughout this work for control and simulation.

a. Full model. With a static magnetic field B_0 aligned to the NV axis and a linearly polarized microwave (MW) field $B_{1,\text{MW}}(t)$ applied orthogonally, the coupled NV-nuclear system is described by

$$H_{\text{NV}} = D(S_z^2 - \frac{2}{3}) + \gamma_e B_0 S_z + \gamma_e B_{1,\text{MW}}(t) S_x + \sum_i \vec{S} \cdot A_i \cdot \vec{I}_i - \sum_i \gamma_i B_0 I_{iz} + \sum_i Q_i (I_{iz}^2 - \frac{2}{3}), \quad (\text{C1})$$

where $D = 2.87$ GHz is the zero-field splitting, \vec{S} ($S = 1$) are the NV electronic spin operators, \vec{I}_i are nuclear spins (^{14}N , selected ^{13}C) with gyromagnetic ratios γ_i , A_i are hyperfine tensors, and Q_i are nuclear quadrupole terms. Throughout, energies are expressed in angular-frequency units.

b. Two-level reduction and secular approximation. We restrict the electronic subspace to the qubit manifold $\{|0_e\rangle, |-1_e\rangle\}$ and apply a secular approximation *with respect to the large electronic Zeeman splitting* (valid for $B_0 \gtrsim 0.5$ T). This removes fast electron spin-flip terms outside the qubit manifold while *retaining transverse hyperfine components* (A_{xz}, A_{yz}) as small but relevant perturbations (hyperfine misalignment). In this basis the

Hamiltonian is

$$H_{\text{NV}} = H_e + |0_e\rangle\langle 0_e| \otimes H_0 + |-1_e\rangle\langle -1_e| \otimes H_{-1}, \quad (\text{C2})$$

with

$$H_e = \frac{\Lambda_s}{2} \sigma_z + \gamma_e B_{1,\text{MW}}(t) \frac{\sigma_x}{\sqrt{2}}, \quad (\text{C3})$$

$$H_0 = - \sum_i \gamma_i B_0 I_{iz} + \sum_i Q_i (I_{iz}^2 - \frac{2}{3}), \quad (\text{C4})$$

$$H_{-1} = - \sum_i \gamma_i B_0 I_{iz} + \sum_i (A_{i,zz} I_{iz} + A_{i,xz} I_{ix} + A_{i,yz} I_{iy}) + \sum_i Q_i (I_{iz}^2 - \frac{2}{3}), \quad (\text{C5})$$

where Λ_s is the $|0_e\rangle \leftrightarrow |-1_e\rangle$ transition frequency. Due to hyperfine coupling, Λ_s depends on the nuclear configuration, i.e. the *electron detuning is transition dependent*.

c. Hyperfine misalignment and nuclear-axis rotation.

To diagonalize the time-independent part of H_{-1} for each nucleus, we rotate the nuclear axes by angles (ϕ_i, θ_i) determined by the local hyperfine tensor [78]:

$$\tan \phi_i = \frac{A_{i,xz}}{A_{i,yz}}, \quad \tan \theta_i = \frac{\sqrt{A_{i,xz}^2 + A_{i,yz}^2}}{A_{i,zz} + \gamma_i B_0}. \quad (\text{C6})$$

Defining rotated operators $(I'ix, I'iy, I'iz)$, the nuclear Hamiltonians in the auxiliary and computational subspaces become

$$H_0 = - \sum_i \gamma_i B_0 (I'iz \cos \theta_i - I'iy \sin \theta_i) + \sum_i Q_i (I'iz^2 - \frac{2}{3}), \quad (\text{C7})$$

$$H_{-1} = - \sum_i \omega_i I'iz + \sum_i Q_i (I'iz'^2 - \frac{2}{3}), \quad (\text{C8})$$

$$\omega_i = \sqrt{(A_{i,zz} + \gamma_i B_0)^2 + A_{i,xz}^2 + A_{i,yz}^2}. \quad (\text{C9})$$

d. Small-angle expansion (misalignment as a perturbation). For weakly misaligned ^{13}C (small θ_i selected by geometry), we expand to first order in θ_i :

$$H_0 \approx - \sum_i \gamma_i B_0 I'iz + \sum_i Q_i (I'iz'^2 - \frac{2}{3}) + \sum_i \gamma_i B_0 \theta_i I'iy, \quad (\text{C10})$$

$$H_{-1} \approx - \sum_i \omega_i I'iz + \sum_i Q_i (I'iz'^2 - \frac{2}{3}), \quad (\text{C11})$$

where the first-order correction appears only in the auxiliary subspace (consistent with the perturbative analysis of Chen *et al.* [51]), and higher-order terms are negligible for $\theta_i \ll 1$.

e. Interaction picture (pre-RWA). Before applying the rotating-wave approximation, we move to the interac-

tion picture with respect to $H_0^{\text{ref}} = \frac{\Lambda_s}{2} \sigma_z - \sum_i \gamma_i B_0 I_{iz} + \sum_i Q_i (I_{iz}^2 - \frac{2}{3})$. The total Hamiltonian retains its block structure,

$$H_{\text{NV}}(t) = H_e^{(I)}(t) + H_{eN}^{(I)}(t) + |0_e\rangle\langle 0_e| \otimes H_0^{(I)}(t) + |-1_e\rangle\langle -1_e| \otimes H_{-1}^{(I)}(t), \quad (\text{C12})$$

where the electron term explicitly depends on the nuclear configuration $\mathbf{m} \equiv (m_N, \{m_{C_i}\})$:

$$H_e^{(I)}(t) = \frac{\gamma_e B_{1,\text{MW}}(t)}{\sqrt{2}} \sum_{\mathbf{m}} [\sigma_x \cos(\Lambda(\mathbf{m})t) - \sigma_y \sin(\Lambda(\mathbf{m})t)] \otimes |\mathbf{m}\rangle\langle \mathbf{m}|, \quad (\text{C13})$$

with configuration-dependent transition frequencies

$$\Lambda(\mathbf{m}) = \Lambda_s - \left[m_N (\gamma_N B_0 - \omega_N) + \sum_{i=1}^M m_{C_i} (\gamma_{C_i} B_0 - \omega_{C_i}) \right], \quad (\text{C14})$$

where Λ_s denotes the electron transition frequency (containing the Zero field Splitting and Zeeman splitting) and each ω_i denotes the nuclear precession frequency in the computational manifold as defined in Eq. (C9).

f. Electron-nuclear modulation. Residual transverse hyperfine components $(A_{i,xz}, A_{i,yz})$ generate a weak, microwave-induced modulation of the nuclear degrees of freedom. To first order in the misalignment angles θ_i from Eq. (C6), this coupling takes the form

$$H_{eN}^{(I)}(t) = -\sqrt{2} \gamma_e \frac{B_{1,\text{MW}}(t)}{2} [q_x \sin(\Lambda_s t) + q_y \cos(\Lambda_s t)] \otimes \sum_i \theta_i [I'ix \cos(\delta_i t - \phi_i) + I'iy \sin(\delta_i t - \phi_i)], \quad (\text{C15})$$

where $\delta_i = \omega_i - \Lambda_s$ are the beat frequencies between the electronic transition and the nuclear precession modes, and ϕ_i are the azimuthal angles defined in Eq. (C6).

g. Nuclear terms in the interaction picture. Under the interaction picture defined by $H_0^{\text{ref}} = \frac{\Lambda_s}{2} \sigma_z - \sum_i \gamma_i B_0 I_{iz} + \sum_i Q_i (I_{iz}^2 - \frac{2}{3})$, the residual nuclear Hamiltonians acquire only slow, hyperfine-induced modulations. In the auxiliary ($|0_e\rangle$) and computational ($|-1_e\rangle$) manifolds, they read

$$H_0^{(I)}(t) \approx \sum_i \gamma_i B_0 \theta_i [I'iy \cos(\gamma_i B_0 t) + I'ix \sin(\gamma_i B_0 t)], \quad (\text{C16})$$

$$H_{-1}^{(I)}(t) \approx - \sum_i (\omega_i - \gamma_i B_0) I'iz, \quad (\text{C17})$$

where $\omega_i = \sqrt{(A_{i,zz} + \gamma_i B_0)^2 + A_{i,xz}^2 + A_{i,yz}^2}$ is the effective nuclear precession frequency in the computational manifold. No direct term proportional to $B_{1,\text{MW}}$ appears, since the microwave field couples only to the electronic spin; all microwave-induced nuclear dynamics arise in-

directly through the electron-nuclear modulation term $H_{eN}^{(I)}(t)$ in Eq. (C15).

h. RWA in the detuning interaction picture. Preemptively, we define the configuration-dependent detunings

$$\Delta_e(\mathbf{m}) = \omega_{\text{MW}} - \Lambda(\mathbf{m}), \quad (\text{C18})$$

where $\Lambda(\mathbf{m})$ is the configuration-dependent electron transition frequency (cf. Eq. (C14)). We drive the electron at ω_{MW} . Let $B_{1,\text{MW}}(t) = 2B_1 \cos(\omega_{\text{MW}}t)$ and define the on-resonance electron Rabi frequency $\Omega = \gamma_e B_1 / \sqrt{2}$. Using the product-to-sum identity $\cos \alpha \cos \beta = \frac{1}{2}[\cos(\alpha - \beta) + \cos(\alpha + \beta)]$ and $\cos \alpha \sin \beta = \frac{1}{2}[\sin(\beta + \alpha) + \sin(\beta - \alpha)]$, the electron interaction-picture drive $\propto \sigma_x \cos[\Lambda(\mathbf{m})t] - \sigma_y \sin[\Lambda(\mathbf{m})t]$ splits into a slow (difference-frequency) piece and explicit counter-rotating (sum-frequency) pieces:

$$\begin{aligned} H_e^{(\text{full})}(t) = \Omega \sum_{\mathbf{m}} \left\{ \underbrace{[\sigma_x \cos(\Delta_e(\mathbf{m})t) - \sigma_y \sin(\Delta_e(\mathbf{m})t)]}_{\text{slow (near-resonant)}} \right. \\ \left. + [\sigma_x \cos((\omega_{\text{MW}} + \Lambda(\mathbf{m}))t) - \sigma_y \sin((\omega_{\text{MW}} + \Lambda(\mathbf{m}))t)] \right\} \otimes |\mathbf{m}\rangle\langle\mathbf{m}|. \quad (\text{C19}) \end{aligned}$$

The *rotating-wave approximation* (RWA) keeps only the slow terms and discards the counter-rotating block in Eq. (C19), yielding

$$\boxed{H_e^{(\text{RWA})}(t) = \Omega \sum_{\mathbf{m}} [\sigma_x \cos(\Delta_e(\mathbf{m})t) - \sigma_y \sin(\Delta_e(\mathbf{m})t)] \otimes |\mathbf{m}\rangle\langle\mathbf{m}|.} \quad (\text{C20})$$

i. Electron-nuclear modulation, with explicit counter-rotating terms. For the MW-induced modulation term (cf. Eq. (C15)),

$$\begin{aligned} -\sqrt{2}\gamma_e \frac{B_{1,\text{MW}}(t)}{2} [q_x \sin(\Lambda_s t) + q_y \cos(\Lambda_s t)] \\ \otimes \sum_i \theta_i [I'ix \cos(\delta_i t - \phi_i) + I'iy \sin(\delta_i t - \phi_i)], \quad (\text{C21}) \end{aligned}$$

insert $B_{1,\text{MW}}(t) = 2B_1 \cos(\omega_{\text{MW}}t)$ and use the same product-to-sum identities. This produces a slow component at the difference frequency $\Delta_e = \omega_{\text{MW}} - \Lambda_s$ and explicit fast (counter-rotating) components at the sum

frequency $\omega_{\text{MW}} + \Lambda_s$:

$$\begin{aligned} H_{eN}^{(\text{full})}(t) = \underbrace{-\Omega [q_x \sin(\Delta_e t) + q_y \cos(\Delta_e t)]}_{\text{slow (near-resonant in the electron sector)}} \quad (\text{C22}) \\ \otimes \sum_i \theta_i [I'ix \cos(\delta_i t - \phi_i) + I'iy \sin(\delta_i t - \phi_i)] \\ - \underbrace{\Omega [q_x \sin((\Lambda_s + \omega_{\text{MW}})t) + q_y \cos((\Lambda_s + \omega_{\text{MW}})t)]}_{\text{counter-rotating (fast)}} \quad (\text{C23}) \end{aligned}$$

$$\otimes \sum_i \theta_i [I'ix \cos(\delta_i t - \phi_i) + I'iy \sin(\delta_i t - \phi_i)]. \quad (\text{C24})$$

Under an MW-only drive near the electronic resonance ($\omega_{\text{MW}} \simeq \Lambda_s$) and with no RF near any nuclear Larmor frequency, the counter-rotating blocks in Eqs. (C19) and (C24) oscillate at $\omega_{\text{MW}} + \Lambda(\mathbf{m})$ and $\omega_{\text{MW}} + \Lambda_s$, respectively, and are dropped by the RWA. The retained (slow) electron-nuclear term is therefore

$$\boxed{H_{eN}^{(\text{RWA})}(t) = -\Omega [q_x \sin(\Delta_e t) + q_y \cos(\Delta_e t)] \otimes \sum_i \theta_i [I'ix \cos(\delta_i t - \phi_i) + I'iy \sin(\delta_i t - \phi_i)].} \quad (\text{C25})$$

As $|\omega_{\text{MW}} - \omega_i| \gg \Omega$ in the MW-only regime, these mixed-frequency factors are far off-resonant for the nuclei and contribute primarily small second-order (AC Zeeman/Bloch-Siegert-like) dispersive shifts.

j. Nuclear terms under the rotating-wave approximation. The nuclear Larmor and hyperfine precession frequencies ($\gamma_i B_0, \omega_i \sim \text{MHz}$) are much slower than the microwave drive ($\omega_{\text{MW}} \sim \text{GHz}$), leading to a clear separation of timescales. Within this limit, the oscillatory components of $H_0^{(I)}(t)$ in Eq. (C16) average out on the microwave period and produce only weak, off-resonant nuclear mixing of order $\gamma_i B_0 \theta_i / \Omega \ll 1$. To first order, the auxiliary-manifold term may thus be neglected on the timescale of typical MW pulses.

For longer gate durations ($\sim 1\text{-}2 \mu\text{s}$) or for strongly coupled, misaligned ^{13}C spins, these residual oscillations can accumulate small but coherent nuclear rotations (amplitude $\lesssim 2\theta_i$), and $H_0^{(I)}(t)$ should then be retained in quantitative simulations. By contrast, the computational-manifold Hamiltonian remains purely static, contributing only configuration-dependent phase shifts through the hyperfine detuning ($\omega_i - \gamma_i B_0$).

TABLE I: Physical parameters used for the nuclear spins in the NV- ^{14}N - $^{13}\text{C}_1$ - $^{13}\text{C}_2$ register simulation.

Parameter	^{14}N ($I=1$)	$^{13}\text{C}_1$ ($I=\frac{1}{2}$)	$^{13}\text{C}_2$ ($I=\frac{1}{2}$)
$\gamma/2\pi$ (MHz/T)	3.077	10.71	10.71
A_{zz} (MHz)	-2.14	2.281	-1.011
A_{\perp} (MHz)	0.00	0.240	0.014
Q (MHz)	-5.01	0.00	0.00

Accordingly, under the RWA the nuclear sector becomes

$$\begin{aligned}
 H_0^{(\text{RWA})}(t) &\approx \sum_i (\gamma_i B_0 \theta_i) [I'_{iy} \cos(\gamma_i B_0 t) \\
 &\quad + I'_{ix} \sin(\gamma_i B_0 t)] \approx 0 \\
 H_{-1}^{(\text{RWA})} &\approx - \sum_i (\omega_i - \gamma_i B_0) I'_{iz}.
 \end{aligned}
 \tag{C26}$$

For fast MW gates, the first line is negligible and the nuclei evolve quasi-statically, modulating the electron

transition through slow, configuration-dependent frequency shifts. For longer gates or stronger misalignments, the auxiliary wobble term $H_0^{(\text{RWA})}(t)$ can generate measurable, coherent nuclear motion. Since their effect is typically small, we neglect these residual nuclear terms in the model Hamiltonian for demonstrative purposes; any coherent nuclear response then arises solely from the microwave-mediated coupling $H_{eN}^{(\text{RWA})}(t)$.

Appendix D: NV-register simulation parameters

The NV electronic spin ($S=1$), with gyromagnetic ratio $\gamma_e/2\pi = 28.024$ GHz/T, couples to one intrinsic ^{14}N nucleus and two proximate ^{13}C spins through anisotropic hyperfine tensors A_{zz} and A_{\perp} , with an external magnetic field $B_0 = 0.45$ T aligned with the NV axis. The nuclear-spin parameters listed in Table I correspond to typical experimental ranges reported in Refs. [51, 79].